Chemical Engineering Journal 496 (2024) 153974

Contents lists available at ScienceDirect

Chemical Engineering Journal

journal homepage: www.elsevier.com/locate/cej

A systematic investigation of PVDF-HFP in perovskite solar cells for improved space mission reliability

Seoungjun Ahn [a], Wei-Hao Chiu [b], Wei-Chen Chu [a], Pei-Yu Chen [a], Ting-Han Lin [b], Kun-Mu Lee [a,b,c,d,*]

[a] Department of Chemical and Materials Engineering, Chang Gung University, Taoyuan 33302, Taiwan
[b] Center for Sustainability and Energy Technologies, Chang Gung University, Taoyuan 33302, Taiwan
[c] College of Environment and Resources, Ming Chi University of Technology, New Taipei City 24301, Taiwan
[d] Division of Neonatology, Department of Pediatrics, Chang Gung Memorial Hospital, Linkou, Taoyuan 33305, Taiwan

ARTICLE INFO

Keywords:
Perovskite solar cell
PVDF-HFP
Space environment
Vacuum degradation
Gamma ray
Renewable energy

ABSTRACT

Metal halide perovskites have sparked considerable interest in photovoltaic (PV) research due to their exceptional optoelectronic attributes. The remarkable power conversion efficiency (PCE), superior power-to-weight ratios, adaptability to flexible substrates, and robust radiation tolerance position perovskite solar cells (PSCs) as a compelling option for futuristic space PV applications. In this study, we enhance the stability of PSCs by incorporating the additive poly (vinylidene fluoride-co-hexafluoropropylene) (PVDF-HFP) into the perovskite composition and evaluate their performance under vacuum and gamma-ray irradiation conditions. The fluorine content in PVDF-HFP establishes strong hydrogen bonding with the perovskite's organic cations and coordination bonds with Pb^{2+} ions, facilitating effective defect mitigation within the perovskite matrix. PVDF-HFP PSCs showed a marked increase in PCE of 22.54 %, comparing to 19.85 % for the pristine one. Furthermore, PVDF-HFP PSCs retained 70 % of their initial PCE after 600 h in a vacuum environment (2×10^{-7} torr). Additionally, it exhibited strong resilience to gamma-ray exposure. These results indicate that the integration of PVDF-HFP as an additive in perovskite solar cells significantly enhances their stability and performance in the harsh space condition.

1. Introduction

Organic-inorganic hybrid perovskite solar cells (PSCs) possess outstanding photoelectric properties, including adjustable band gap, high carrier mobility, small exciton binding energy, low cost, and efficient solution-based fabrication routes [1–3]. Recent research in perovskite-based solar cells has demonstrated generation efficiencies exceeding 26 % [4]. Moreover, with the implementation of additional passivation techniques, PSCs have already surpassed 1000 h of stability [5,6]. Consequently, ongoing investigations indicate that PSCs are poised to become the next-generation solar cells, potentially replacing silicon-based solar cells, garnering significant attention globally. The key to achieving highly efficient and stable PSCs lies in the nature of the perovskite films. Among the various perovskite compositions, methylammonium lead triiodide ($MAPbI_3$) and formamidinium lead triiodide ($FAPbI_3$) are widely used. However, $MAPbI_3$ exhibits poor stability and a low open-circuit voltage (Voc). To address these limitations, various metals, organic cations, and halogens can be incorporated to replace corresponding elements or ions. For instance, formamidinium (FA) and cesium (Cs) can replace methylammonium (MA), broadening the absorption range. This substitution enables the attainment of a band gap suitable for visible light wavelengths, leading to high power conversion efficiency (PCE) [7,8]. FA-Cs compounds exhibit exceptional thermal and light stability, particularly under high-intensity solar radiation [9,10]. These properties, coupled with the promising inherent crystal stability, contribute to achieving high PCE in perovskite solar cells. Recent studies have highlighted the significant influence of crystallinity, grain size, and grain boundary of perovskite crystals on the increase of PCE [11,12].

Polymer additives, particularly those with abundant functional groups, play a pivotal role in forming stable and reliable interactions with perovskite grains, facilitating the formation of high-quality perovskite films. Polymer-based defect passivation strategies have been widely adopted to enhance perovskite solar cells performance,

---

* Corresponding author at: Department of Chemical and Materials Engineering, Chang Gung University, Taoyuan 33302, Taiwan.
E-mail address: KMLee@mail.cgu.edu.tw (K.-M. Lee).

https://doi.org/10.1016/j.cej.2024.153974
Received 20 April 2024; Received in revised form 29 June 2024; Accepted 11 July 2024

with various additives utilized for this purpose [13,14]. During the annealing process, fluorinated polymer additives, such as PVDF(Poly (Vinylidenefluoride)) [15–17], PVDF-HFP(poly(vinylidenefluoride-co-hexafluoropropylene) [18,19], and PVDF-TrFE(polyvinylidene fluoride–trifluoroethylene) [20], interact with organic cations and Pb^{2+} ions, retarding perovskite crystallization and promoting the formation of high-quality films. PVDF-based enhances perovskite solar cells by providing effective surface passivation, improving stability, optimizing interfaces for charge transport, and maintaining mechanical integrity. These properties make PVDF a valuable material in advancing the performance and durability of perovskite-based photovoltaic technologies [21]. This improvement is attributed to having more fluorine (F) content in PVDF-HFP, which associates with hydrogen atoms to form H-F bonds. These bonds stabilize the phase structure and encourage a preferred crystal orientation. Additionally, PVDF-HFP plays a crucial role in suppressing non-radiative recombination rates at the interface, enhancing carrier transport, and maintaining the integrity of the perovskite layer through its hydrophobic nature [19]. Furthermore, these additives act as connecting bridges at grain boundaries, passivating vacancies in the perovskite lattice, which effectively inhibits nonradiative recombination and enhances the Voc of PSCs. Incorporating fluorinated compounds within the perovskite layer or as an interlayer on top of perovskite facilitates the formation of hydrogen-fluorine bonds with organic cations, thereby improving perovskite moisture resistance and enhancing the thermal resilience of the device [15,22].

Space-based solar cells face numerous environmental threats, including vacuum, atomic oxygen, high-energy radiation (such as X and gamma rays), charged particle radiation (such as high-energy electrons and protons), plasma, temperature extremes, and thermal cycling. Long-term exposure to these hazards is expected to degrade the materials and components of solar cells, leading to device failures. Understanding the impact of these extreme conditions on the service life of solar cells and uncovering degradation mechanisms are crucial for evaluating the suitability of PSCs for space applications [23–25]. Recent research has shown that perovskite films undergo rapid decomposition at low pressure ($5x10^3$ Pa), accelerating phase-segregation and transition starting from the grain boundaries. This process is accompanied by outgassing and defect formation, which further accelerates ion migration across the device, involving ions like Li^+, Au, I^-, and Br^- [23]. Under vacuum conditions typical of space environments, the emission of organic gas components like CH_3NH_2, HI, CH_3I, NH_3, and I_2 from $MAPbI_3$ powder, and $HN{=}CHNH_2$, HI, HCN, and NH_3 from $FAPbI_3$ powder, was observed under both dark and light conditions at 10^{-4} Pa. The presence of light accelerates the outgassing rates. These organic gases have the potential to contaminate surfaces within the line of sight, impacting the optical properties of spacecraft, payload surfaces, and overall spacecraft performance [26]. The vacuum stability of PSCs is contingent upon the chosen fabrication techniques. While the $MAPbI_3$ film, synthesized using a dimethyl formamide (DMF)-based precursor solution and subjected to dark and vacuum storage, deteriorates into PbI_2, subsequently forming metallic lead (Pb_0) and I_2 ions, the film fabricated from a combination of DMF and dimethyl sulfoxide (DMSO) precursor exhibits minimal degradation under identical conditions [27]. Furthermore, the triple-cation perovskite film demonstrates markedly slower degradation rates compared to $MAPbI_3$ under equivalent vacuum and illumination conditions, owing to its superior thermal stability [28,29]. On the other hand, Gamma rays, with their high penetrating ability, pose a significant threat to space-based solar cells. Over the 20 years of space utilization, solar cells can accumulate a large dose of gamma radiation, significantly impacting their performance. While recent studies have demonstrated the high resistance of mixed cation PSCs to gamma rays, it has been shown that mixed-halide PSCs are less suitable for space applications due to halide phase segregation induced by gamma ray exposure [30,31]. The inverted structure perovskite solar cell demonstrated excellent gamma-ray radiation hardness under gamma ray irradiation with an accumulated dose of 2.3 Mrad, surpassing that of crystalline silicon solar cells [32]. There is little research on the operational stability of perovskite solar cells when deployed in space environments. Furthermore, there is scarce investigation into potential solutions for addressing the aforementioned issues.

Here in this work, we demonstrate that PSCs fabricated using a one-step spin-coating technique with a PVDF-HFP concentration of 0.15 mg/ml exhibit enhanced stability in space-related conditions. The incorporation of PVDF-HFP into the perovskite solution yields films with smoother surfaces, increased grain sizes, and overall improved film quality. Moreover, under vacuum conditions, pristine perovskite films increase defects due to the evaporation of cations, whereas PVDF-HFP perovskite films demonstrate mitigation of perovskite degradation attributed to the fluorine atoms in PVDF-HFP. Furthermore, PVDF-HFP PSCs exhibit minimal changes even under gamma ray exposure. Therefore, by demonstrating the relationship between physical changes and device performance, we argue that the addition of PVDF-HFP leads to more stable perovskite solar cells in space environments.

2. Results and discussion

In this study, we investigate the structural, morphological, optical, electronic, and photovoltaic properties of perovskite solar cells examining in space conditions, such as vacuum or gamma ray environment. Throughout this paper, perovskite film containing PVDF-HFP are labeled as “PVDF-HFP perovskite film,” and the one without this additive as “pristine perovskite film.” Similarly, “PVDF-HFP PSC” and “pristine PSC” indicate the PSC with and without PVDF-HFP, respectively.

Fig. 1 (a) displays a pristine perovskite film with small crystals (average grain size of 0.331 ± 0.133 μm in Figure (c)), whereas Fig. 1 (b) shows a PVDF-HFP perovskite film with larger crystals (average grain size of 0.529 ± 0.240 μm in Figure (d)), indicating a 52.8 % increase. This suggests that the interaction between PVDF-HFP and perovskite encourages the formation of larger perovskite grains during crystal formation [15]. PVDF-HFP brings about a passivation effect by binding with uncoordinated Pb^{2+} ions in perovskite, mitigating surface defects and grain boundaries in perovskite films. This results in smoother and more uniform surfaces while also regulating the crystallization process of perovskite materials [33]. The introduction of PVDF-HFP polymer appears to preserve the integrity of the perovskite structure, potentially serving as a bridging agent between grain boundaries. The interactions between ferroelectric polymers and perovskite crystals seem to enhance the tensile forces among perovskite grains, resulting in the formation of larger grains and a more compact morphology [34]. The RMS (root-mean-square) roughness values, shown in Fig. 1 (e) and (f), are 25.0 nm for pristine perovskite film and 23.7 nm for PVDF-HFP perovskite film, respectively. Incorporating PVDF-HFP leads to a flatter surface of perovskite films, making it more suitable for the spin-coating of the hole transporting layer (HTL), and consequently improving charge transfer [35]. Finally, the examination of crystalline characteristics through XRD for both pristine and PVDF-HFP perovskite films is shown in Fig. 1 (h) and (g). Both films exhibit typical tetragonal crystal structures with (110), (112), (202), (220), (310), (224), and (314) planes of perovskite film. The crystallinity of the (110) plane gradually increases in the PVDF-HFP perovskite film. Additionally, it also demonstrates an increase in grain size, shown in Table S1. The polymer addition significantly influences crystal growth, enhancing uniform growth and minimizing voids during the annealing processs [19]. Consequently, the addition of PVDF-HFP leads to enhanced crystal grains, improved crystallinity, and effective suppression of non-radiative recombination, as evident in the increased fill factor (FF) detailed in Table 1.

X-ray photoelectron spectroscopy (XPS) measurements were carried out to inspect the coordinate bonding between PVDF-HFP and perovskite. In Fig. 2 (a), the results showed that the main peaks for the pristine perovskite films at 142.28 eV (Pb $4f_{5/2}$) and 137.38 eV (Pb $4f_{7/2}$) shifted to lower binding energies of 142.11 eV (Pb $4f_{5/2}$) and 137.21 eV (Pb $4f_{7/}$

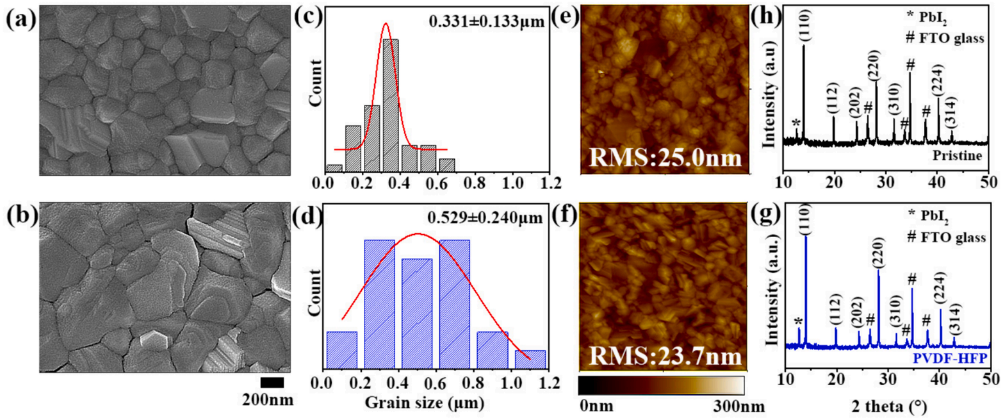

Fig. 1. Comparative display of different perovskite films: FE-SEM top-view images, grain size distributions, AFM images, and XRD patterns. The upper set (a, c, e, g) shows for pristine films, while the lower set (b, d, f, h) shows for PVDF-HFP perovskite films, respecitively.

Table 1
Photovoltaic characteristics of FTO/SnO_2/perovskite/Spiro-OMeTAD/Ag devices.

Sample	Voc (V)	Jsc (mA/cm^2)	FF (%)	PCE (%)
Pristine	1.069 ± 0.021 **(1.097)**	24.38 ± 0.23 **(24.25)**	73.01 ± 1.43 **(74.58)**	18.86 ± 0.72 **(19.84)**
	1.070 ± 0.019 **(1.097)**	24.38 ± 0.23 **(24.24)**	73.08 ± 1.42 **(74.64)**	18.87 ± 0.72 **(19.85)**
PVDF-HFP	1.116 ± 0.014 **(1.137)**	24.64 ± 0.15 **(24.83)**	77.21 ± 1.19 **(79.74)**	21.35 ± 0.59 **(22.52)**
	1.116 ± 0.014 **(1.138)**	24.64 ± 0.15 **(24.80)**	77.26 ± 1.16 **(79.86)**	21.36 ± 0.57 **(22.54)**

The performance metrics of the champion device are indicated in parentheses. The average values and standard deviations are calculated from 18 devices.

$_2$) when PVDF-HFP perovskite film. Similarly, in Fig. 2 (b), the I 3d$_{3/2}$ and I 3d$_{5/2}$ peaks in the PVDF-HFP perovskite film at 629.28 eV and 617.78 eV shifted to lower binding energies compared to the pristine at 629.31 eV and 617.91 eV, respectively. Additionally, the presence of the C-2F peak at 289.10 eV in the PVDF-based perovskite film further demonstrated the incorporation of PVDF-HFP in Fig. 2 (c). These XPS results collectively confirm that the PVDF-HFP effectively binds and passivates with Pb^{2+}, reducing electron trap density. Consequently, the reduction in electron trap density leads to improved charge carrier transport and overall enhanced electrical properties of the perovskite films, confirming the passivation effect of PVDF-HFP and its role in enhancing film quality and performance [15,36].

In Fig. 3 (a), the pristine PSCs attained a PCE of 19.85 %, with an open-circuit voltage (Voc) of 1.097 V, a short-circuit current density (Jsc) of 24.24 mA/cm^2, and a FF of 74.64 %. In contrast, the PVDF-HFP PSCs demonstrated a significantly enhanced PCE, with 22.54 %, a Voc of 1.138 V, a Jsc of 24.80 mA/cm^2, and a FF of 79.86 %. The photovoltaic parameters are summarized in Table 1 and a box plot of the PCE distribution and of pristine and PVDF-HFP PSCs is shown in Fig. 3 (b). Quite evidently, the PVDF-HFP PSCs experienced a significant improvement, primarily attributable to the enhancements in Voc and FF (an increase of about 41 mV and 5.22 %, respectively). This aligns with the findings of the previous report [16,19]. The improvement in FF is attributed to the decreasing R_S and increasing R_{Sh}, as illustrated in Fig. S1, while enhancing Voc may involve reducing the trap density within the perovskite film.

The short-term device stability was evaluated by conducting maximum power-point tracking (MPPT) measurements under AM 1.5G illumination in ambient air conditions (as shown in Fig. S2 a and b).

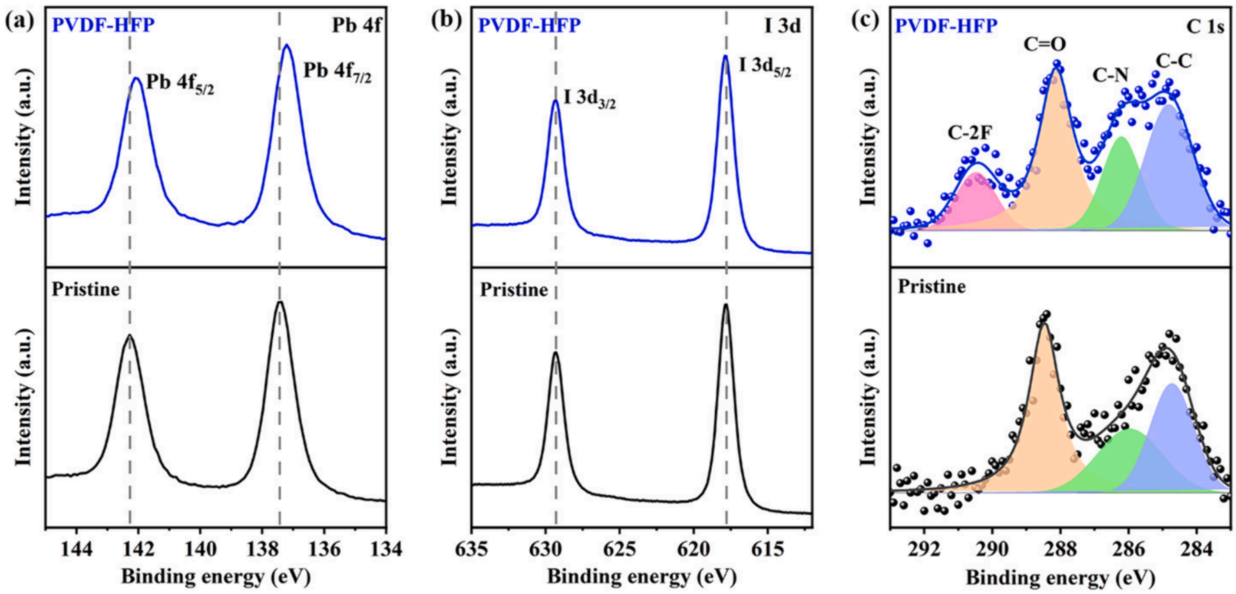

Fig. 2. XPS spectra (a) Pb 4f, (b) I 3d, and (c) C 1 s of the pristine and PVDF-HFP perovskite film.

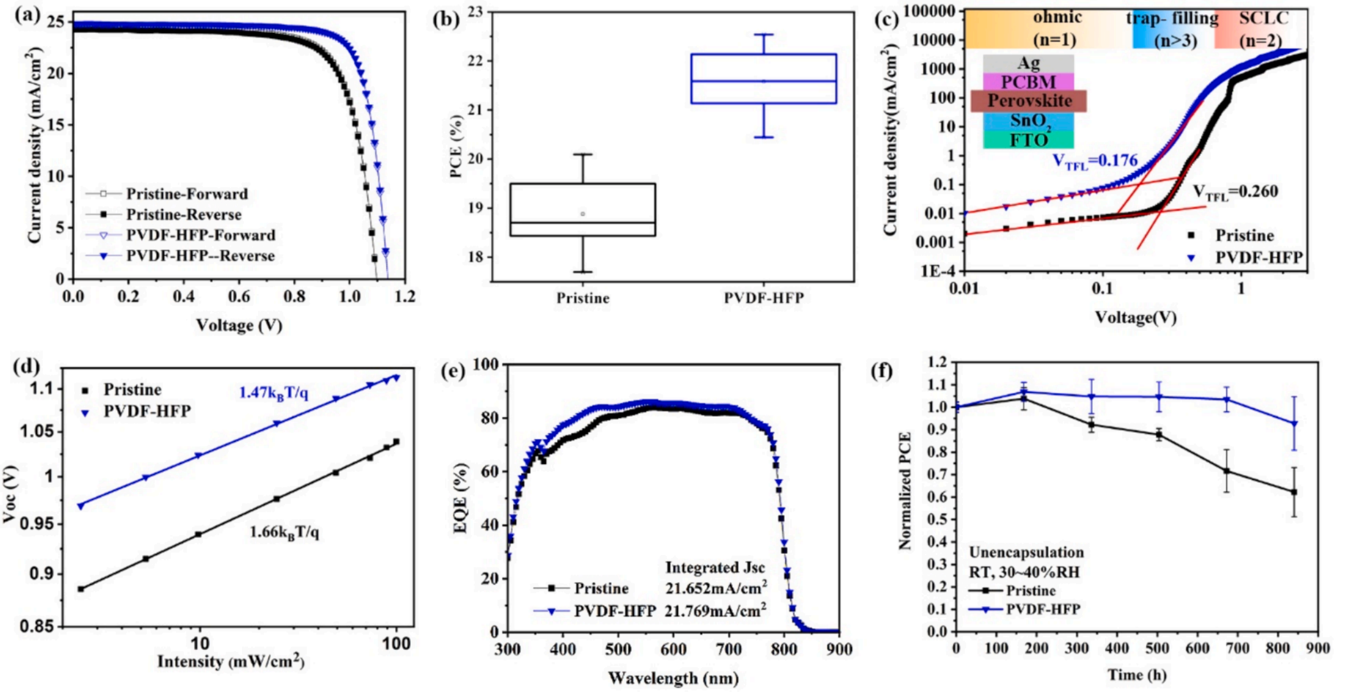

Fig. 3. (a) J-V curves of pristine and PVDF-HFP perovskite solar cells(PSCs) measured under simulated AM 1.5G. (b) The average power conversion efficiency (PCE) distribution of pristine and PVDF-HFP PSCs. (c) Space charge limited current model (SCLC) measurement of electron-only devices with pristine and PVDF-HFP perovskite films. (d) VOC-versus light intensity for the pristine and PVDF-HFP PSCs. (e) EQE spectra of the best-performing devices of pristine and PVDF-HFP PSCs. (f) Long-term stability of the corresponding unencapsulated perovskite solar cells in an ambient environment with 30 ~ 40 % relative humidity at RT (25 °C).

PVDF-HFP PSCs exhibited superior stability and enhanced power output in comparison to pristine PSCs, resulting in a stabilized PCE of 22.0 % (equivalent to 97.6 % of the initial PCE). To quantitatively analyse the defect density of perovskite films, we employ the space-charge-limited current (SCLC) technique, constructing electron-only devices for this purpose. The SCLC curves of the PSCs exhibited three distinct regions in Fig. 3 (c). First, in the ohmic region at low bias, the relationship between current density and electric field was linear. Second, at intermediate bias, there was a significant increase in current due to the trap-filled limit region. Third, at high bias potential, there was a trap-free SCLC region. In trap filling region, the trap density was continuously filled until the trap-filled limit voltage (V_{TFL}). The trap-state density (N_{traps}) can be described by the following Equation (1) [37].

$$N_{traps} = \frac{2V_{TFL}\varepsilon_0\varepsilon}{eL^2} \tag{1}$$

where N_{traps}, V_{TFL}, ε_0, ε, e, L are trap-state density, the trap-filled limit voltage, vacuum permittivity ($\varepsilon_0 = 8.8 \times 10^{-12}$F/m), the relative dielectric constant of perovskite, electron charge ($e = 1.6 \times 10^{-19}$C), the film thickness of perovskite (500 nm), respectively. From the fitting results, shown in Table S2, the trap densities in the PVDF-HFP perovskite film were 2.08 x 10^{15} cm^{-3}, which is lower than the 3.09 x 10^{15} cm^{-3} found for the pristine one. The charge mobility was further extracted using the Mott-Gurney Law (Equation (2): [38]

$$\mu = \frac{8J_D L^3}{9\varepsilon_0\varepsilon V^2} \tag{2}$$

where J_D is the current density and V is the applied voltage. The charge mobility is estimated to be 5.09 × 10^{-4} and 1.22 × 10^{-3} cm^2/Vs for pristine and PVDF-HFP perovskite films, respectively. Furthermore, by integrating the calculated values for carrier mobility and lifetime, the diffusion lengths were determined through the application of a specific equation.

Furthermore, by integrating the acquired values of carrier mobility and carrier lifetime, diffusion lengths were determined using the following Equation (3) [39].

$$L_D = \sqrt{\frac{k_B T}{e} \times \mu\tau} \tag{3}$$

where L_D is diffusion length, k_B is Boltzmann's constant, T is temperature, τ is carrier lifetimes, μ is carrier mobility.

$$L_D(Pristine) = \sqrt{0.026V \times 5.09 \times 10^{-4} cm^2V^{-1}S^{-1} \times 59.50ns} \\ = 8.87 \times 10^{-2}\mu m \tag{4}$$

$$L_D(PVDF-HFP) = \sqrt{0.026V \times 1.22 \times 10^{-3} cm^2V^{-1}S^{-1} \times 81.57ns} \\ = 1.60 \times 10^{-1}\mu m \tag{5}$$

These findings suggest a lower defect density and enhanced transport characteristics of the PVDF-HFP perovskite film, aligning with the computed data in Equations (4) and (5). Fewer defects are essential for achieving efficient and stable perovskite solar cells due to reduced charge recombination and superior transport properties to achieve higher Voc [40,41] and FF [38]. The observed reduction in electron trap density values in PVDF-HFP perovskite films provides confirmation that the fluorine (F) atoms within the PVDF-HFP effectively passivate the uncoordinated Pb^{2+} defects present in the perovskite films. The strong electronegativity of F atoms in PVDF-HFP enables them to donate the lone electron pair of the F atom to the empty 6p orbital of Pb^{2+}. This suggests that PVDF-HFP can effectively passivate defects in the perovskite film [15,19]. To understand the mechanism and evaluate the probability of carrier recombination inside the devices by using light intensity dependent V_{OC} and J_{SC} measurement in Fig. 3 (d) and Fig. S3, the plots of Voc versus natural logarithmic light intensity have been implemented and abide by the following Equation (6):

$$\frac{Voc}{\ln\left(\frac{I}{I_o}+1\right)} = nk_BT/q \tag{6}$$

where I, I_0, n, k_B, T and q are light intensity, initial light intensity, ideality factor, Boltzmann constant, absolute temperature and elementary charge, respectively. nk_BT/q is the value of the linear fitting slope and in connection with defect-assisted recombination. Generally, the value of n closer to 1 suggests the less defect-assisted recombination. The PVDF-HFP PSCs, with a slope of 1.47 kBT/q, show significantly lower recombination compared to the pristine device's 1.66 kBT/q. This suggests that PVDF-HFP effectively reduces trap-assisted recombination, moving closer to the ideal 1 kBT/q. Consequently, PVDF-HFP enhances defect passivation, diminishes charge recombination, and improves overall photovoltaic performance and stability [17,42]. The external quantum efficiency (EQE) was further analyzed to validate the Jsc. As depicted in Fig. 3 (e), the spectral response of the PVDF-HFP PSCs demonstrated a slight improvement in the range of 350 to 700 nm, suggesting enhanced conversion of EQE into current. This improvement is attributed to the overall quality of the perovskite crystal, rather than the p-i or n-i interfaces [17]. The integrated Jsc, obtained through EQE spectra, increased from 21.65 to 21.76 mA/cm^2. This trend aligns well with the corresponding J-V curves, indicating currents of 24.24 and 24.80 mA/cm^2, respectively. Before discussing the device stability in space condition, the stability of unencapsulated device under ambient condition with temperature 25 °C, relative humidity 30 ∼ 40 % is shown in Fig. 3 (f). The PCE of PVDF-HFP PSCs shows the slow degradation and maintains more than 92 % of the initial value at 850 h. In contrast, the performance of pristine PSCs severely degrades, maintaining only 62 % of the initial PCE at 850 h. Due to the abundant hydrophobic F and the long-chain structure of PVDF-HFP, a robust hydrophobic barrier layer is formed on the surface of PVDF-HFP perovskite film. This layer significantly enhances moisture resistance, making PVDF-HFP perovskite films more effective in preventing the penetration of water molecules and thereby improving the humidity stability of perovskite PSCs [17].

We conduct a study on the stability of pristine and PVDF-HFP PSCs in space environments. Specifically, we investigate the morphology and optical analyses of perovskite films and PSCs by exposing them to a vacuum environment of 2x10^{-7} torr. In Fig. 4 (a), the long-term stability is monitored for the PSCs in a vacuum environment without encapsulation. After 600 h, the PCE of PVDF-HFP PSCs remained at 70 %, while the pristine PSCs dramatically decreased to only 32 %. Notably, the most significant change in PV parameters is the reduction in Voc with a substantial decrease of 24 % PVDF-HFP PSCs and 47 % pristine PSCs, as shown in Fig. S4. These findings suggest that PVDF-HFP contributes to enhanced stability in the vacuum environment, as evidenced by the sustained efficiency and less pronounced deterioration in key parameters compared to the pristine PSCs. Among the various potential mechanisms leading to a reduction in PCE, such as recombination losses, optical losses, series resistive losses, etc., recombination losses, whether occurring at the interface or within the bulk, are particularly significant. This is because they exert a substantial impact on both the Voc and FF [23,43,44]. The Voc loss analysis, shown in Fig. 4 (b) and Table S3, is carried out provides insights into the reasons behind the decrease in the Voc of PSCs. The mathematical relationship depicted in the image outlines the methodology for calculating the Voc loss in perovskite solar cells, as defined by the Shockley-Queisser limit. This theoretical framework stipulates that Voc loss comprises three distinct components [45].

$$\begin{aligned} q\Delta V &= Eg - qVoc \\ &= (Eg - qVoc^{SC}) + (qVoc^{SC} - qVoc^{rad}) + (qVoc^{rad} - qVOC) \\ &= (Eg - qVoc^{SC} \\ &\quad + q\Delta Voc^{SC}) + \Delta qVoc^{rad} + \Delta qVoc^{non-rad}) = q(\Delta V1 + \Delta V2 + \Delta V3) \end{aligned} \tag{7}$$

In principle, ΔV1 is due to the thermodynamic loss, ΔV2 is radiative recombination loss, and ΔV3 is non-radiative recombination loss. In the equation (7), q denotes the elementary charge, and ΔV represents the

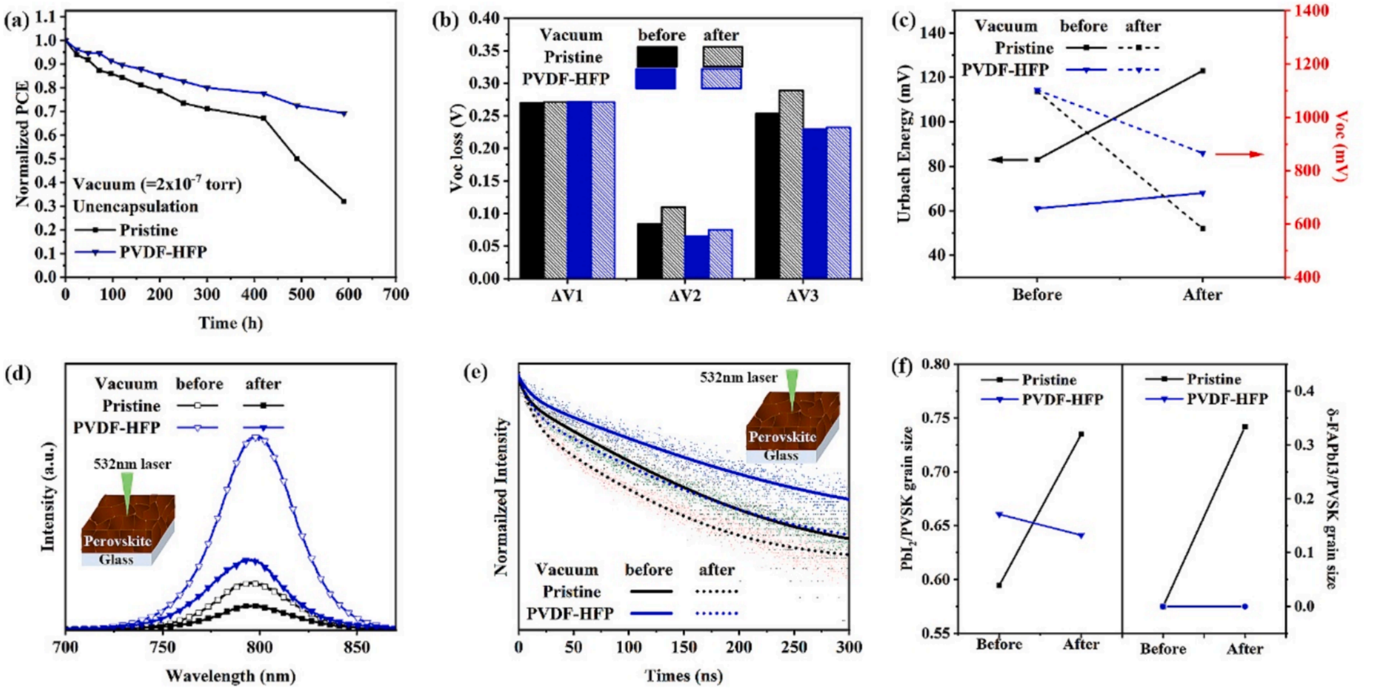

Fig. 4. (a) Long-term stability of the corresponding perovskite solar cells without encapsulation, (b) the radiative and non-radiative Voc loss of the perovskite solar cells pristine and PVDF-HFP, (c) the Urbach energy of pristine and PVDF-HFP perovskite films in an 2x10^{-7} torr vacuum condition, (d) photoluminescence (PL) spectra and (e) Normalized time-resolved photoluminescence (TRPL) decay profiles of the pristine and PVDF-HFP perovskite film, (f) PbI$_2$/PVSK and δ-FAPbI$_3$/PVSK grain size ratio.

total open-circuit voltage loss. By measuring the bandgap energy (Eg), the Voc at the Shockley-Queisser limit (Voc^{SQ}), and the Voc with full radiative recombination (Voc^{rad}), researchers can calculate each of these losses. These values are pivotal for understanding and optimizing the performance of perovskite solar cells. The bandgap energy (Eg) is a fundamental property of the solar cell material, while Voc^{SQ} and Voc^{rad} are specific voltages that reflect the ideal and actual energy conversion scenarios, respectively. The values of ΔV1 before vacuum exposure for both pristine and PVDF-HFP PSCs are very close, measuring 0.270 V and 0.272 V, respectively. Similarly, the after vacuum ΔV1 values for both cases are 0.271 V, indicating a similarity to the initial values. This is attributed to the absence of any significant change in the bandgap. ΔV2 occurs when photoexcited charge carriers (electrons and holes) recombine [43]. Therefore, this observation is associated with the quality of the perovskite film. In the case of pristine PSCs, there is a noticeable increase in Voc loss, from 0.084 V before vacuum exposure to 0.110 V after vacuum. However, for PVDF-HFP PSCs, a slight improvement is observed, with increasing from 0.065 V to 0.075 V. ΔV3, which represents nonradiative recombination loss, occurs when charge carriers recombine without emitting a photon. This phenomenon is attributed to bulk defects, buried bottom interfaces, and top interfaces [46,47]. In the case of pristine PSCs, there is an increase in ΔV3 from 0.253 V to 0.289 V. For PVDF-HFP PSCs, the increment is less pronounced, going from 0.229 V to 0.232 V. Consistent with previous findings, PVDF-HFP PSCs demonstrates improvements in both radiative and nonradiative recombination. Furthermore, even under vacuum, PVDF-HFP PSCs exhibits greater stability compared to pristine. It is noteworthy that perovskite films are known to undergo evaporation of MA^+ ions in a vacuum state [23]. The surface-coated PVDF-HFP and the hydrogen bond interactions between F and FA^+/MA^+ effectively impede the volatilization of ammonium salts [17]. Therefore, PVDF-HFP appears to inhibit the evaporation of MA^+. To investigate trap states and gain deeper insights into the optoelectronic properties of our fabricated perovskite films, we conduct an analysis of Urbach energy (Eu), photoluminescence (PL), and time-resolved photoluminescence (TRPL). The Eu serves as a significant parameter reflecting the crystallinity, defects, and optoelectronic characteristics of a material. It obeys the Urbach energy Equation (8), governing the relationship between absorbance (α) and energy (hv) near the optical band edge. The determination of Eu involves analyzing the slope adjacent to the optical band edge [48].

$$\alpha = \alpha_0 \exp(\frac{h\upsilon}{E_u}) \tag{8}$$

In Fig. 4 (c), for the pristine perovskite film, the Eu is calculated to be 83 meV, whereas for PVDF-HFP perovskite film, it is notably smaller, at 61 meV. This reduction aligns with the earlier results from the SCLC measurements, indicating a decrease in the defect density of the film. After 600 h in a vacuum condition, the Eu value for pristine PSCs increases to 123 meV, while for PVDF-HFP PSCs, it is measured at 68 meV (in Fig. S5). Despite an increase in defects for both films after vacuum, PVDF-HFP PSCs exhibits significantly greater stability. Consequently, in the case of PVDF-HFP PSCs, the decrease in Voc is also observed to be less pronounced. This can be attributed to PVDF-HFP PSCs having lower trap-assisted recombination, which accounts for the diminished reduction in Voc compared to the pristine sample. PL measurements are performed on pristine and PVDF-HFP perovskite films coated on glass substrates, as depicted in Fig. 4(d). It is evident from the figure that the PL intensity of the PVDF-HFP perovskite film is considerably enhanced. It is known that the presence of more trap states in a film subjected to vacuum conditions leads to an increase in photoluminescence intensity for perovskite films [49]. Under vacuum conditions, the intensity of PVDF-HFP perovskite film is observed to be higher than that of the pristine, indicating superior crystal quality, a correlation supported by XRD results and contributing to an enhanced Voc (in Fig. S6 and Table S1). Additionally, the emission peak position remains unchanged with the incorporation of polymer into the perovskite solution, signifying uniform bandgap values across all perovskite films. This suggests the suppression of non-radiative recombination rates with polymer addition. As previously explained in the context of Voc loss (ΔV3), the diminished nonradiative recombination signifies a reduction in trap states and defects within the perovskite films [19].

The TRPL decay measurement is performed on pristine and PVDF-HFP perovskite film on glass substrate in Fig. 4(e). Through TRPL measurement, the electron-hole recombination time is affected by the film crystallinity and its defects can be fitted by a bi-exponential rate law as below Equation (9):

$$I_{PL}(t) = A_1 e^{(-\frac{t}{\tau_1})} + A_2 e^{(-\frac{t}{\tau_2})} \tag{9}$$

The TRPL data is represented by $I_{PL}(t)$, with τ_1 and τ_2 denoting the lifetimes for fast and slow recombination, respectively, while A_1 and A_2 represent their relative amplitudes. The fitting parameters derived from the analysis are summarized in Table2. The swift decay component (τ_1) is associated with non-radiative recombination linked to surface defects, whereas the prolonged component (τ_2) is attributed to radiative recombination related to bulk properties. For the pristine sample, the values of τ_1 and τ_2 are 8.26 ns and 81.55 ns, respectively, whereas PVDF-HFP perovskite film exhibits faster decay (τ_1 = 9.49 ns) and slower decay (τ_2 = 112.98 ns) components. This indicates a suppression of trap-assisted recombination and an enhancement in the quality of the bulk perovskite. Under vacuum conditions, the τ_1 and τ_2 values for the pristine perovskite film are 6.46 ns and 67.95 ns, respectively, while PVDF-HFP perovskite film shows faster and slower decay components of 8.29 ns (τ_1) and 86.17 ns (τ_2), respectively. The improved FF and Voc observed in PVDF-HFP PSCs, as outlined in Table 1, align with increased perovskite crystal size, fused grain boundaries, preferred (1 1 0) grain growth, and the ferroelectric properties of PVDF copolymers. These factors collectively reduce nonradiative recombination sites and enhance charge separation. The decrease in trap-assisted recombination is attributed to the lower defect concentration, indicating superior electronic quality in PVDF-HFP perovskite film [17,18,49]. To qualitatively investigate the impact of vacuum conditions on the decomposition of the perovskite film, we present a figure illustrating representative XRD peak area ratios between the decompositions, as shown in Fig. 4 (f), detailed in Fig. S6 and Table S1. For the pristine perovskite film, there is a significant increase in the PbI_2/PVSK (perovskite) grain size ratio within a vacuum environment. This observation provides evidence of an augmented presence of PbI_2 in the Pristine perovskite film, signifying the evaporation of MA^+ during the vacuum process. Conversely, PVDF-HFP perovskite film exhibits a similar ratio, suggesting minimal changes in the film during vacuum exposure. Furthermore, in the pristine film, the presence of a peak corresponding to δ-$FAPbI_3$ is identified. These newly formed phases are non-photoactive within the perovskite absorbance range and are expected to induce Jsc losses [49]. These findings, support the assertion that vacuum conditions induce distinct changes in the pristine perovskite film, evident from increased PbI_2 content and the emergence of non-photoactive phases. In contrast, the PVDF-HFP perovskite film remains comparatively stable under the same conditions [23,50].

To elucidate the cation evaporation phenomenon under vacuum conditions, we employ top-view and cross-section SEM imaging to scrutinize alterations in the perovskite film. Additionally, energy

Table 2
Summary of the parameters from fitting to the TRPL decay.

Sample	Vacuum	A_1	τ_1 (ns)	A_2	T_2(ns)	$\tau_{average}$(ns)
Pristine	Before	0.30	8.26	0.70	81.55	59.50
	After	0.41	6.46	0.59	67.95	42.45
PVDF-HFP	Before	0.30	9.49	0.70	112.98	81.57
	After	0.47	8.29	0.53	86.17	49.18

dispersive X-ray spectroscopy (EDS) is utilized to probe the atomic percentages of N, C, Pb, Br, and I of the perovskite film. SEM analysis before and after vacuum exposure reveals significant morphological differences in perovskite films. In Fig. 5 (a) and b, pristine perovskite films exhibit increased porosity and crack formation after vacuum, resulting in uneven surfaces and a notable rise in RMS values (in Fig. S7), indicating morphological transformation [51]. In contrast, PVDF-HFP perovskite films maintain a dense structure with minimal RMS increase in Fig. 5 (c) and (d), demonstrating superior stability. In Fig. 5(e) and (f), small-sized perovskite crystals in pristine perovskite film align vertically in SEM top-view. After vacuum, fragmentation or increased boundaries between perovskite grains are observed. Conversely, PVDF-HFP perovskite film shows no significant difference before and after vacuum. Detailed EDS analysis reveals a substantial reduction in the N and C ratio of the perovskite film at (β) region compared to (α), indicating cation evaporation and an increase in Pb and I ratios on the surface [23]. After vacuum, PVDF-HFP perovskite film shows a slight decrease in C and N, but maintains superior uniformity and stability compared to pristine perovskite film, attributed to strong hydrogen bonding. Overall, PVDF-HFP perovskite films demonstrate enhanced stability under vacuum conditions, suggesting potential for space applications. Perovskite degradation accelerates under vacuum, leading to decomposition, phase-segregation, and cation release. However, PVDF-HFP films exhibit enhanced stability compared to pristine perovskite films, indicating suitability for vacuum condition.

To singularly evaluate the effects of gamma radiation on PSCs, our initial step involved subjecting FTO substrates to gamma rays to monitor resultant alterations. The Fig. S8 illustrate a pronounced reduction in light transmittance within the 300–750 nm wavelength spectrum upon gamma ray exposure of the FTO glass. This phenomenon is attributed to ionization processes, which generate free charge carriers that subsequently become ensnared in existing vacancies or impurities [30,52]. Notably, the sheet resistance of the FTO appears to remain stable despite exposure to gamma radiation, as shown in Fig. S8. Consequently, this result focuses on the transmittance changes in the FTO substrates and their potential effects on PSC performance. In the context of evaluating the radiation resilience of the devices, Fig. 6(a) presents the use of PSCs for this purpose. Meanwhile, Fig. 6(b) and (c) compare the experimentally obtained PCE and Voc against their theoretically calculated counterparts, PCE_{cal} and Voc_{cal}, respectively. The evaluation of the device's PCE alterations is conducted through the application of a specific equation (10): [30]

$$PCE_{cal} = \frac{Jsc_{cal} * Voc_{(0Krad)} * FF_{(0Krad)}}{P_{light}} * 100\% \tag{10}$$

Assuming that gamma rays induce only a glass darkening effect, the device's Voc and FF are unaffected. Therefore, we can use initial values measured before the radiation exposure for the estimation of the maximal achievable PCE_{cal}. The Jsc_{cal} is estimated by the integration of the modelled EQE_{cal} over the standard AM1.5G spectrum. The calculation of Jsc_{cal} and Voc_{cal} are detailed in the Supplementary note (in Figs. S9 and S10). Both pristine and PVDF-HFP PSCs exhibit a significant decrease in PCE following gamma ray exposure. However, the PCE change in PVDF-HFP PSCs closely aligns with the variation in PCE_{cal}, indicating that the efficiency changes in PVDF-HFP PSCs are attributed to the decrease in substrate transparency. In the case of pristine PSC, the

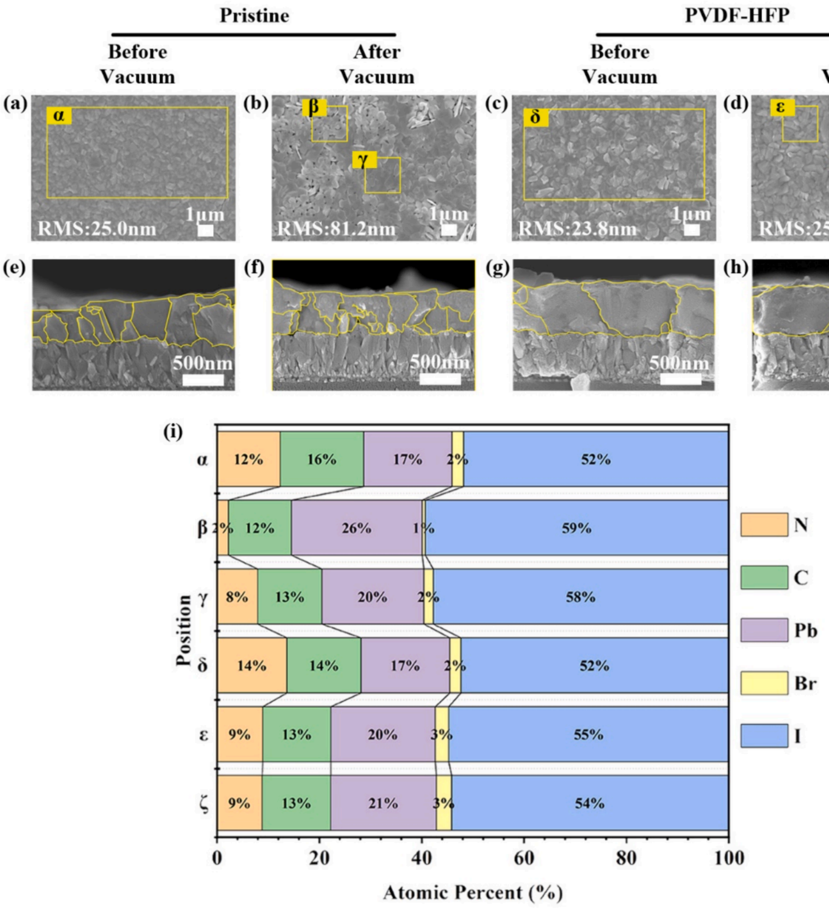

Fig. 5. Energy dispersive X-ray spectroscopy (EDS) spectra acquired in scanning electron microscopy (SEM) at the top view and cross section SEM images of the pristine and PVDF-HFP perovskite film. (a), (e) pristine perovskite film before Vacuum, (b), (f) pristine perovskite film after vacuum, (c), (g) PVDF-HFP perovskite film before vacuum (d), (h) PVDF-HFP perovskite film after vacuum, and (i) Atomic percent of the Pristine and PVDF-HFP perovskite film from EDS.

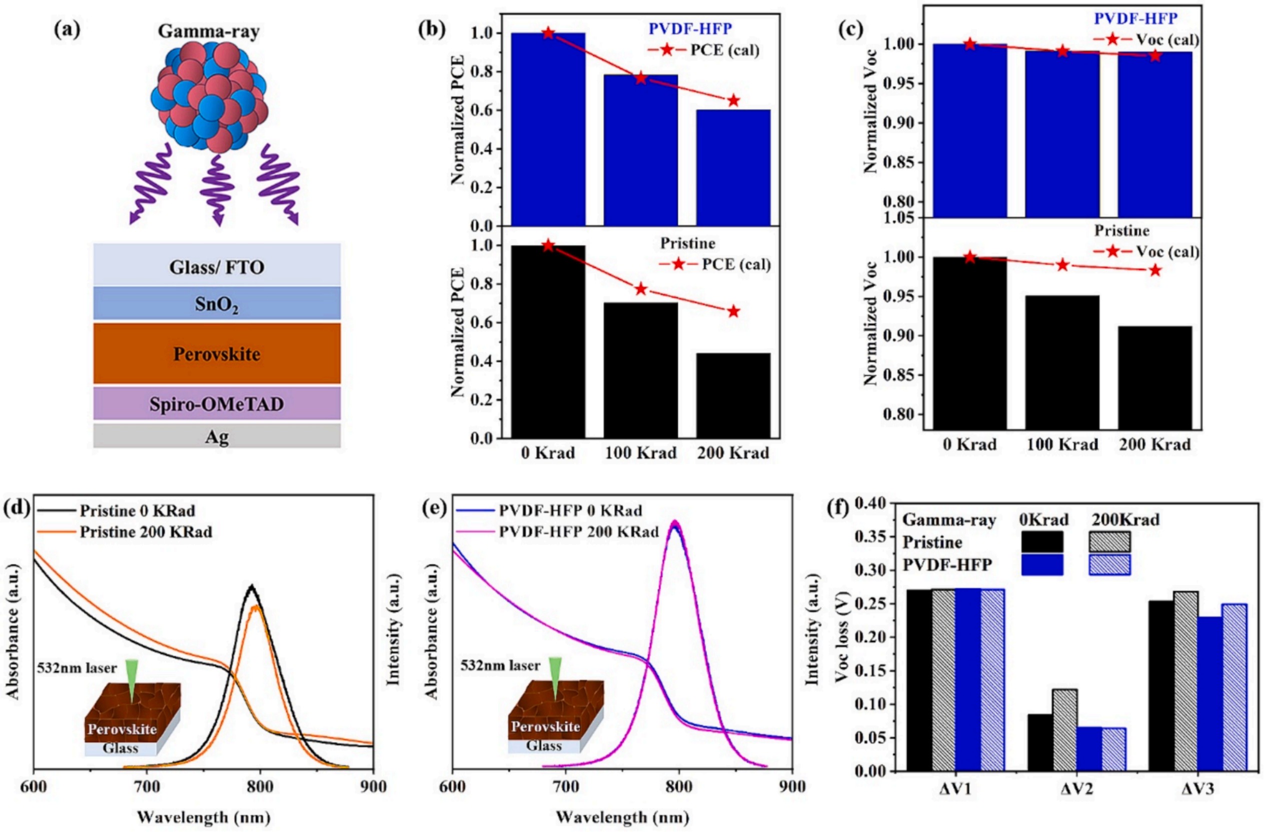

Fig. 6. (a) Schematic diagram of PSC exposed to gamma ray. (b) PCE and (c) Voc evolution of PSCs under gamma ray radiation. Red lines show the expected behavior in case gamma rays induce only substrate darkening without damaging the PV stack. (d) UV−vis absorption and (e) PL spectra of pristine and PVDF-HFP perovskite films under gamma ray radiation. (f) Voc loss measurement of the pristine and PVDF-HFP PSCs before and after gamma ray radiation. (For interpretation of the references to colour in this figure legend, the reader is referred to the web version of this article.)

decrease in PCE is greater than that of PCE_{cal}, indicating degradation under gamma ray exposure mainly due to intrinsic radiation-induced processes rather than because of the decrease in substrate transparency. As shown in Fig. 6 (c), the Voc of the pristine PSC decreases under gamma ray exposure, and a significant decrease in FF is also observed (in Figs. S11 and S12). Particularly, the significant decrease in Voc and FF supports the conclusion of trap formation and massive charge carrier recombination in the active layer and/or at some functional interface [53]. We investigated the conductivity of SnO_2 and Spiro-OMeTAD layers under gamma ray exposure in Fig. S13. SnO_2 was unaffected by gamma ray exposure, while Spiro-OMeTAD exhibited decreased conductivity after exposure. As previously demonstrated, triple cation perovskite undergoes rapid degradation under gamma ray exposure [30,54,55]. However, when PVDF-HFP is added, it exhibits significantly improved stability under gamma ray. Fig. 6 (d) and (e) depict the changes in PL intensity for pristine and PVDF-HFP perovskite films under gamma ray exposure. For the pristine perovskite film, the intensity decreases after gamma ray exposure, while the PVDF-HFP perovskite film shows similar intensity before and after gamma ray exposure. These results indicate an increase in defects in the pristine perovskite film after gamma ray exposure. Similarly, the Voc loss results in Fig. 6 (f) show a significant increase in ΔV2 for pristine after gamma ray exposure, while PVDF-HFP PSC shows minimal change. This suggests that pristine perovskite solar cells degrade under gamma ray exposure. XRD analysis reveals an increase in PbI_2 peaks and grain size after gamma ray exposure for pristine. Moreover, boundaries appear more distinct in SEM images, and AFM results show a slight increase in RMS (in Figs. S14–S16, and Table S4). However, PVDF-HFP PSCs show little impact from gamma ray exposure. ΔV3 increases for both pristine and PVDF-HFP PSCs, indicating issues with the perovskite film and spiro-OMeTAD interface. The PVDF-HFP perovskite film demonstrates robust resistance to gamma ray exposure, surpassing that of the pristine perovskite film. Thus, PVDF-HFP perovskite films exhibit strong resilience to vacuum conditions and gamma ray exposure, rendering them promising candidates for space applications.

3. Conclusion

In this study, we investigated the effects of additive PVDF-HFP into perovskite films to improve photovoltaic performance and operational stability in space environments. PVDF-HFP PSCs showed a significant enhancement in PCE, reaching up to 22.54 % compared to the pristine 19.85 %, an improvement of over 11 %. The improved photovoltaic performance is attributed to enhanced carrier lifetimes and reduced charge transport resistance. Additionally, the additive of PVDF-HFP had substantial effects on perovskite film morphology, enhancing coverage and smoothness, increasing crystal size, and reducing grain boundaries. Furthermore, PVDF-HFP PSCs maintained 70 % of their PCE over 600 h in a vacuum condition of $2x10^{-7}$ torr, while pristine cells dropped to below 30 %. The additive of PVDF-HFP prevents cation evaporation and maintains a more stable perovskite film under vacuum conditions. Gamma-ray exposure experiments result showed a decrease in transmittance of FTO glass substrate, leading to reduce both PVDF-HFP and pristine perovskite solar cells on glass substrates, leading to reduced PCE. However, the PCE reduction in PVDF-HFP perovskite solar cells was solely attributed to a decrease in Jsc due to reduced transmittance of the substrate, while for pristine perovskite solar cell, an increase in defects within the perovskite film was observed after gamma-ray exposure, more losses were incurred. Thus, PVDF-HFP perovskite films exhibit strong resilience to vacuum condition and gamma-ray exposure, making them promising candidates for space applications. Future research in our group is planned to focus on studying PVDF-HFP perovskite solar cells under environments closely resembling space environments.

4. Experimental Section/Methods

4.1. Materials

The CBD SnO_2 material, Tin(II) chloride dihydrate (98 %) and Thioglycolic acid (98 %) was acquired from Sigma-Aldrich. Urea was acquired from J.T.Baker. Potassium carbonate (K_2CO_3) (99 %) was acquired from Acros. The solvents Dimethylformamide (DMF), Chlorobenzene (CB), and isopropanol (IPA) were procured from Tedia, while Dimethyl sulfoxide (DMSO) at 99 % purity was sourced from Echo Chemical Co., Ltd. Lead (II) Iodide (PbI_2) was acquired from TCI, and Formamidinium Iodide (FAI), Methylammonium Iodide (MAI), and Methylammonium bromide (MABr), 2-phenylethylammonium (PEAI) were purchased from FMPV®. Additional reagents such as cesium iodide (CsI), 4-*tert*-butylpyridine (4-tBP), and lithium-bis (trifluoromethylsulfonyl) imide (Li-TFSI) were obtained from Aldrich, while Spiro-OMeTAD was purchased from Ruilong.

4.2. Device fabrication

The FTO substrates were subjected to ultrasonic washing with detergent, deionized water, acetone, and 2-propanol for 10 min each, followed by treatment with UV-ozone for 20 min, before use. For SnO_2 ETL (electron transport layer) deposition, the FTO substrate and the CBD SnO_2 solution, prepared by mixing 625 mg of urea, 625 μL of HCl, 13 μL of TGA, and 137.5 mg of $SnCl_2{\cdot}2H_2O$ per 400 mL of DI water, were loaded into a glass reaction vessel and reacted 3 h at 70 °C for 2 times. After completion of the reaction, the SnO_2 deposited FTO substrate was removed from the reaction vessel and cleaned via with DI water. The FTO/SnO_2 substrate was annealed in an ambient environment (RH 60 %) at 180 °C for 60 min. This was followed by spin-coating 10 mM K_2CO_3 in DI water, the solution at 3000 rpm for 30 sec and annealing at 105 °C for 10 min. Before perovskite deposition, the FTO/SnO_2 substrate was UV-ozone treated again and pumped inside a dry air glovebox (RH 0.1 %). Subsequently, the triple perovskite layer was deposited using a one-step spin-coating method. The 1.5 M $Cs_{0.05}(FA_{0.75}MA_{0.20})PbI_{2.95}Br_{0.05}$ perovskite precursor solution was prepared by mixing CsI (16.26 mg), MABr (14 mg), MAI (19.8 mg), FAI (161.2 mg), PbI_2 (576.3 mg) dissolving in the mixed solvent of 1 ml DMF/DMSO (4:1 in v:v). Additionally, PVDF-HFP perovskite film is 0.15 mg/mL PVDF-HFP polymer molecule was dissolved in the DMF/DMSO solvent as the additive into the perovskite precursor. The perovskite precursor was spin-coated on FTO/SnO_2/K_2CO_3 at 1,000 and 5,000 rpm for 10 s and 30 s, respectively. During the second stage, 100 μl toluene was dropped onto the surface at 16th second, and the substrate was annealed at 70 °C for 10 min and then 135 for 60 min in ambient air with 0.1 % humidity. As a hole-transporting material, Spiro-OMeTAD (80 mg), 4-tBP (28.5 μl), and LiTFSI (17.5 μl) were dissolved in 1 mL of CB, and spin-coated at 2000 rpm for 30 s onto the perovskite film. Finally, a counter electrode of approximately 100 nm thickness of Ag was deposited by thermal evaporation using a shadow mask with an active area of 0.09 cm^2 (3 mm × 3 mm).

4.3. Characterization

The AM 1.5G solar simulator (SS-F5-3A, ENLI Technology Co. Ltd.) was used as the irradiation light source for the current density–voltage (J–V) measurements. The illumination intensity of 100 mW/cm^2 was calibrated before cell performance measurement. The J–V characteristics of the PSCs under the illumination of AM 1.5G simulated sunlight were obtained by applying the external potential bias to the cell and measuring the photocurrent output with a Keithley model 2400 digital source meter. The External Quantum Efficiency (EQE) (QE-R-3011, ENLI Technology Co. Ltd.) calibrated with a single-crystalline silicon reference cell was used for the EQE measurements. Voc loss measurement was performed by applying external voltage/current sources through the devices (REPS-TEN, Enlitech) The photoluminescence (PL) spectra and time-resolved PL (TRPL) spectra were recorded with a 532 nm diode laser (LDH-D-TA-530, PicoQuant). The TRPL plots were recorded by a time-correlated singlephoton counting (TCSPC) (TimeHarp 260, PicoQuant) spectrometer. Surface morphologies of samples were recorded by a tapping-mode atomic-force microscope (AFM) (NanoScope NS3A system, Digital Instruments) and a field emission scanning electron microscope (FE-SEM) (Hitachi, SU8010). XRD spectrum was obtained using an X-ray diffractometer (D8 130 Focus, Bruker). UV–Vis spectra was measured by a broadband spectrometer (U-4100, HITACHI). Gamma ray radiation stability test was tested by a Gammacell® 3000. X-ray photoelectron spectroscopy (XPS) measurement was carried out on a Thermo-Fisher Scientific K-Alpha X-ray photoelectron spectrometer under a pressure of 5.0×10^{-9} Pa.

CRediT authorship contribution statement

Seoungjun Ahn: Writing – original draft, Data curation. **Wei-Hao Chiu:** Writing – review & editing, Data curation. **Wei-Chen Chu:** Data curation. **Pei-Yu Chen:** Formal analysis. **Ting-Han Lin:** Software. **Kun-Mu Lee:** Writing – review & editing, Conceptualization.

Declaration of competing interest

The authors declare that they have no known competing financial interests or personal relationships that could have appeared to influence the work reported in this paper.

Data availability

The authors do not have permission to share data.

Acknowledgements

K.-M.L. thanks the support from National Science and Technology Council, Taiwan (Grant Number NSTC 111-2223-E-182-001-MY4), Chang Gung University (URRPD2N0011) and Chang Gung Memorial Hospital, Linkou, Taiwan (CMRPD2M0042).

Appendix A. Supplementary data

Supplementary data to this article can be found online at https://doi.org/10.1016/j.cej.2024.153974.

References

[1] Y. Zhao, K. Zhu, Organic–inorganic hybrid lead halide perovskites for optoelectronic and electronic applications, Chem. Soc. Rev. 45 (3) (2016) 655–689.

[2] Y. Wu, et al., The Impact of Hybrid Compositional Film/Structure on Organic–Inorganic Perovskite Solar Cells, Nanomaterials (basel) 8 (6) (2018).

[3] C.-H. Chiang, et al., The synergistic effect of H2O and DMF towards stable and 20% efficiency inverted perovskite solar cells, Energ. Environ. Sci. 10 (3) (2017) 808–817.

[4] Z. Liang, et al., Homogenizing out-of-plane cation composition in perovskite solar cells, Nature 624 (7992) (2023) 557–563.

[5] S. Bai, et al., Planar perovskite solar cells with long-term stability using ionic liquid additives, Nature 571 (7764) (2019) 245–250.

[6] J. Sanchez-Diaz, et al., Tin perovskite solar cells with >1,300 h of operational stability in N2 through a synergistic chemical engineering approach, Joule 6 (4) (2022) 861–883.

[7] C.-H. Tien, H.-Y. Lai, L.-C. Chen, Methylammonium halide salt interfacial modification of perovskite quantum dots/triple-cation perovskites enable efficient solar cells, Sci. Rep. 13 (1) (2023) 5387.

[8] J. Chen, et al., Highly efficient and stable perovskite solar cells enabled by low-dimensional perovskitoids, Sci. Adv. 8 (4) (2022) eabk2722.

[9] S. Wang, et al., Over 24% efficient MA-free CsxFA1−xPbX3 perovskite solar cells, Joule 6 (6) (2022) 1344–1356.

[10] Q. Guo, et al., Multiple-cation wide-bandgap perovskite solar cells grown using cesium formate as the Cs precursor with high efficiency under sunlight and indoor illumination, PCCP 24 (29) (2022) 17526–17534.

[11] T. Salim, et al., Perovskite-based solar cells: impact of morphology and device architecture on device performance, J. Mater. Chem. A 3 (17) (2015) 8943–8969.

[12] A. Fakharuddin, et al., Perovskite-polymer blends influencing microstructures, nonradiative recombination pathways, and photovoltaic performance of perovskite solar cells, ACS Appl. Mater. Interfaces 10 (49) (2018) 42542–42551.

[13] S. Wang, et al., Polymeric room-temperature molten salt as a multifunctional additive toward highly efficient and stable inverted planar perovskite solar cells, Energ. Environ. Sci. 13 (12) (2020) 5068–5079.

[14] D.H. Kang, C. Ma, N.G. Park, Antiseptic povidone-iodine heals the grain boundary of perovskite solar cells, ACS Appl Mater Interfaces 14 (7) (2022) 8984–8991.

[15] R. Sun, et al., Over 24% efficient poly(vinylidene fluoride) (PVDF)-coordinated perovskite solar cells with a photovoltage up to 1.22 V, Adv. Funct. Mater. 33 (6) (2023) 2210071.

[16] A. Shit, et al., Influence of Poly(Vinylidene fluoride) on photovoltaic performance of interfacially engineered band gap modulated P3TAA-co-P3HT perovskite solar cell at ambient condition, Polymer 185 (2019) 121973.

[17] H. Zheng, et al., Highly efficient and stable perovskite solar cells with strong hydrophobic barrier via introducing poly(vinylidene fluoride) additive, Journal of Energy Chemistry 57 (2021) 593–600.

[18] S. Zhang, et al., PVDF-HFP additive for visible-light-semitransparent perovskite films yielding enhanced photovoltaic performance, Sol. Energy Mater. Sol. Cells 170 (2017) 178–186.

[19] S. Narendhiran, et al., Poly(vinylidene fluoride-co-hexafluoropropylene) additive in perovskite for stable performance of carbon-based perovskite solar cells, Int. J. Energy Res. 46 (2) (2022) 1565–1574.

[20] C. Sun, et al., Enhanced photovoltaic performance of perovskite solar cells using polymer P(VDF-TrFE) as a processed additive, J. Phys. Chem. C 120 (24) (2016) 12980–12988.

[21] B.M. Lefler, et al., Interfacial topochemical fluoridation of MAPbI3 by fluoropolymers, The Journal of Physical Chemistry Letters 14 (21) (2023) 5040–5047.

[22] Z. Yang, et al., High-performance fully printable perovskite solar cells via blade-coating technique under the ambient condition, Adv. Energy Mater. 5 (13) (2015) 1500328.

[23] Y. Jiang, et al., Mitigation of vacuum and illumination-induced degradation in perovskite solar cells by structure engineering, Joule 4 (5) (2020) 1087–1103.

[24] R. Guo, et al., Degradation mechanisms of perovskite solar cells under vacuum and one atmosphere of nitrogen, Nat. Energy 6 (10) (2021) 977–986.

[25] Daly, E.J., et al. Space Environment Analysis: Experience and Trends. in Environment Modeling for Space-Based Applications. 1996.

[26] Finckenor, M.M. and K.K. De Groh, *Space environmental effects*. 2015: NASA ISS Program Science Office.

[27] R.K. Gunasekaran, et al., Revealing the self-degradation mechanisms in methylammonium lead iodide perovskites in dark and vacuum, ChemPhysChem 19 (12) (2018) 1507–1513.

[28] E. Smecca, et al., Stability of solution-processed MAPbI3 and FAPbI3 layers, PCCP 18 (19) (2016) 13413–13422.

[29] J. Yang, et al., Unraveling photostability of mixed cation perovskite films in extreme environment, Adv. Opt. Mater. 6 (2018) 1800262.

[30] A.G. Boldyreva, et al., Unravelling the material composition effects on the gamma ray stability of lead halide perovskite solar cells: MAPbI3 breaks the records, The Journal of Physical Chemistry Letters 11 (7) (2020) 2630–2636.

[31] K. Yang, et al., Radiation tolerance of perovskite solar cells under gamma ray, Org. Electron. 71 (2019) 79–84.

[32] S. Yang, et al., Organohalide lead perovskites: more stable than glass under gamma-ray radiation, Adv. Mater. 31 (4) (2019) 1805547.

[33] W. Feng, et al., Polymer-assisted crystal growth regulation and defect passivation for efficient perovskite light-emitting diodes, Adv. Funct. Mater. 32 (34) (2022) 2203371.

[34] C.-C. Zhang, et al., Polarized ferroelectric polymers for high-performance perovskite solar cells, Adv. Mater. 31 (30) (2019) 1902222.

[35] F. Meng, et al., Hybrid rinse solvent processing highly flat perovskite films on planar substrate, Electrochem. Commun. 91 (2018) 71–74.

[36] X. Jiang, et al., Understanding the role of fluorine groups in passivating defects for perovskite solar cells, Angew. Chem. Int. Ed. 62 (45) (2023) e202313133.

[37] X. Tang, et al., Improvements in efficiency and stability of perovskite solar cells using a cesium chloride additive, ACS Appl. Mater. Interfaces 14 (23) (2022) 26866–26872.

[38] Y. Long, et al., π-π conjugate structure enabling the channel construction of carrier-facilitated transport in 1D–3D multidimensional CsPbI2Br solar cells with high stability, Nano Energy 89 (2021) 106340.

[39] A.A. Zhumekenov, et al., Formamidinium lead halide perovskite crystals with unprecedented long carrier dynamics and diffusion length, ACS Energy Lett. 1 (1) (2016) 32–37.

[40] Z. Guo, et al., High open-circuit voltage of perovskite solar cells: a review, Energ. Environ. Sci. 15 (2022).

[41] D.-Y. Son, et al., Self-formed grain boundary healing layer for highly efficient CH3NH3PbI3 perovskite solar cells, Nat. Energy 1 (7) (2016) 16081.

[42] Y. Su, et al., Acetic acid-assisted synergistic modulation of crystallization kinetics and inhibition of Sn2+ oxidation in tin-based perovskite solar cells, Adv. Funct. Mater. 32 (12) (2022) 2109631.

[43] T.S. Sherkar, et al., Recombination in perovskite solar cells: significance of grain boundaries, interface traps, and defect ions, ACS Energy Lett. 2 (5) (2017) 1214–1222.

[44] Y. Jiang, et al., Boosting the open circuit voltage and fill factor of qdsscs using hierarchically assembled ITO@Cu2S nanowire array counter electrodes, Nano Lett. 15 (5) (2015) 3088–3095.

[45] X. Sun, et al., Efficient inverted perovskite solar cells with low voltage loss achieved by a pyridine-based dopant-free polymer semiconductor, Angew. Chem. Int. Ed. 60 (13) (2021) 7227–7233.

[46] J. Wang, et al., Highly efficient all-inorganic perovskite solar cells with suppressed non-radiative recombination by a Lewis base, Nat. Commun. 11 (1) (2020) 177.

[47] M. Stolterfoht, et al., Visualization and suppression of interfacial recombination for high-efficiency large-area pin perovskite solar cells, Nat. Energy 3 (10) (2018) 847–854.

[48] A.S. Hassanien, A.A. Akl, Influence of composition on optical and dispersion parameters of thermally evaporated non-crystalline Cd50S50−xSex thin films, J. Alloy. Compd. 648 (2015) 280–290.

[49] J. Wang, et al., Profiling photo-induced degradation for operationally perovskite solar cells in space environment, J. Power Sources 512 (2021) 230520.

[50] Y. Liu, et al., Stabilization of highly efficient and stable phase-pure FAPbI3 perovskite solar cells by molecularly tailored 2D-overlayers, Angew. Chem. Int. Ed. 59 (36) (2020) 15688–15694.

[51] R. Guo, et al., Degradation mechanisms of perovskite solar cells under vacuum and one atmosphere of nitrogen, Nat. Energy 6 (2021).

[52] B. Oryema, et al., Effects of low-dose γ-irradiation on the structural, morphological, and optical properties of fluorine-doped tin oxide thin films, Radiat. Phys. Chem. 176 (2020) 109077.

[53] F. Izadi, et al., Effect of interface defects on high efficient perovskite solar cells, Optik 227 (2021) 166061.

[54] L. Gao, et al., Gamma-ray radiation stability of mixed-cation lead mixed-halide perovskite single crystals, Adv. Opt. Mater. 10 (3) (2022) 2102069.

[55] A.G. Boldyreva, et al., γ-ray-induced degradation in the triple-cation perovskite solar cells, The Journal of Physical Chemistry Letters 10 (4) (2019) 813–818.